

Electronic Supplementary Information

Nucleophilic Reactivity of a Mononuclear Cobalt(III)–Bis(*tert*-butylperoxo) Complex

Bongki Shin,[‡] Younwoo Park,[‡] Donghyun Jeong, and Jaeheung Cho*

Department of Emerging Materials Science, DGIST, Daegu 42988, Korea

[‡]These authors contributed equally to this work.

*Corresponding author: jaeheung@dgist.ac.kr

Table of contents:

Experimental section

Table S1-S4

Scheme S1-S2

Figure S1-S19

Experimental Section

Materials. All chemicals obtained from Aldrich Chemical Co. were the best available purity and used without further purification unless otherwise indicated. The solvents acetonitrile (CH₃CN), methanol (MeOH), and diethyl ether (Et₂O) were passed through solvent purification columns (JC Meyer Solvent Systems) prior to use. D₂O (>99.8% D atom) was purchased from Aldrich Chemical Co. H₂¹⁸O (95% ¹⁸O-enriched) was purchased from ICON Services Inc. (Summit, NJ, USA). [Co^{II}(Me₃-TPADP)(CH₃CN)₂](ClO₄)₂ (**1**-(ClO₄)₂) was synthesized according to literature method.¹

Caution. Perchlorate salts are potentially explosive and should be handled with care!

Instrumentation. UV-vis spectra were recorded on a Hewlett Packard 8454 diode array spectrophotometer equipped with a UNISOKU Scientific Instruments for low-temperature experiments or with a circulating water bath. Electrospray ionization mass (ESI-MS) spectra were collected on a Waters (Milford, MA, USA) Acquity SQD quadrupole Mass instrument, by infusing samples directly into the source using a manual method. The spray voltage was set at 2.5 kV and the capillary temperature at 80 °C. Cold spray ionization mass spectra (CSI-MS) were collected on a JEOL JMS-T100LP 4G spectrometer. The spray voltage was set at 4.2 kV and the capillary temperature at 80 °C. Electron paramagnetic resonance (EPR) spectra were obtained on a JEOL JES- FA200 spectrometer. NMR spectra were measured with Bruker AVANCE III-400 spectrometer at CCRF in DGIST. The effective magnetic moments were determined using the modified ¹H NMR method of Evans at room temperature. A WILMAD[®] coaxial insert (sealed capillary) tubes containing the blank acetonitrile-*d*₃ solvent (with 1.0 % TMS) only was inserted into the normal NMR tubes containing the complexes dissolved in acetonitrile-*d*₃ (with 0.03 % TMS). The chemical shift of the TMS peak (and/or solvent peak) in the presence of the paramagnetic metal complexes was compared to that of the TMS peak (and/or solvent peak) in the inner coaxial insert tube. The effective magnetic moment was calculated using the equation, $\mu = 0.0618(\Delta\nu T/2fM)^{1/2}$, where f is the oscillator frequency (MHz) of the superconducting spectrometer, T is the absolute

temperature, M is the molar concentration of the metal ion, and $\Delta\nu$ is the difference in frequency (Hz) between the two reference signals.² The crystallographic analysis was conducted with a SMART APEX II CCD equipped with a Mo X-ray tube at CCRF in DGIST. Product analysis was performed on a Thermo Fisher Trace 1310 gas chromatograph (GC) system equipped with a flame ionization detector (FID).

Synthesis and Characterization of $[\text{Co}^{\text{III}}(\text{Me}_3\text{-TPADP})(\text{OO}^t\text{Bu})_2]^+$ (2**).** Treatment of $[\text{Co}^{\text{II}}(\text{Me}_3\text{-TPADP})(\text{CH}_3\text{CN})_2](\text{ClO}_4)_2$ (**1**- $(\text{ClO}_4)_2$) (0.05 mmol) with 10 equiv of $t\text{BuOOH}$ in the presence of 2 equiv of TEA in CH_3CN (2 mL) afforded the formation of a dark green solution at 25 °C. Et_2O (40 mL) was added to the resulting solution to yield a dark green powder, which was washed with Et_2O , and dried in vacuo. Dark green powder dissolved in $\text{CH}_3\text{CN}/\text{MeOH}$ ($v/v = 1:1$) with 1 equiv of NaBPh_4 . After the resulting solution was filtered, X-ray crystallographically suitable crystals, $[\text{Co}^{\text{III}}(\text{Me}_3\text{-TPADP})(\text{OO}^t\text{Bu})_2](\text{BPh}_4)(\text{Et}_2\text{O})$ (**2**- $\text{BPh}_4 \cdot \text{Et}_2\text{O}$), were obtained by standing for several days at -40 °C. Crystalline yield: 0.0097 g (40%). Physicochemical data, including UV-vis, ESI-MS, EPR, ^{13}C NMR, and ^1H NMR, were reported in Fig. 1 and Fig. S1. Elemental analysis of **2** was not carried out due to the thermal instability at room temperature. ^{13}C NMR (acetone- d_6 , 400 MHz, 233K) δ , ppm: 162.3 (pyC $_{\alpha}$), 140.3 (pyC $_{\gamma}$), 118.9 (pyC $_{\beta}$), 77.1 (O-C-(CH $_3$) $_3$), 74.9 (O-C-(CH $_3$) $_3$), 71.9 (py-CH $_2$), 66.6, 59.1 (N-CH $_2$ -CH $_2$), 47.6 (N-CH $_3$), 44.3 (N-CH $_3$), 27.8 (O-C-(CH $_3$) $_3$), 26.0 (O-C-(CH $_3$) $_3$); ^1H NMR (acetone- d_6 , 400 MHz, 233K) δ , ppm: 8.13 (t, 1H, pyH $_{\gamma}$), 7.57 (d, 2H, pyH $_{\beta}$), 4.43-4.15 (m, 4H, py-CH $_2$), 3.39 (s, 6H, N-CH $_3$), 3.19-2.42 (m, 8H, N-CH $_2$ -CH $_2$), 2.61 (s, 3H, N-CH $_3$), 1.41 (s, 9H, O-C-(CH $_3$) $_3$), 0.90 (s, 9H, O-C-(CH $_3$) $_3$).

Synthesis and Characterization of $[\text{Co}^{\text{III}}(\text{Me}_3\text{-TPADP})(\text{OO}^t\text{Bu})(\text{N}_3)](\text{ClO}_4)$ (4**- ClO_4).** Treatment of **1**- $(\text{ClO}_4)_2$ (0.05 mmol) with 5 equiv of $t\text{BuOOH}$ and 2 equiv of TEA in the presence of 1.1 equiv of NaN_3 in $\text{CH}_3\text{CN}/\text{MeOH}$ ($v/v = 1:1$, 2 mL) afforded the formation of a green solution at 20 °C. Et_2O (40 mL) was added to the resulting solution to yield a green powder, which was washed with Et_2O , and dried in vacuo. Green powder dissolved in $\text{CH}_3\text{CN}/\text{MeOH}$ ($v/v = 1:1$). After the resulting solution was filtered, X-ray

crystallographically suitable green crystals, $[\text{Co}^{\text{III}}(\text{Me}_3\text{-TPADP})(\text{OO}^t\text{Bu})(\text{N}_3)](\text{ClO}_4)$ (**4-ClO₄**), were also obtained by standing for several days at $-40\text{ }^\circ\text{C}$. Crystalline yield: 0.0093 g (42%). Anal. Calcd for $\text{C}_{18}\text{H}_{33}\text{ClCoN}_7\text{O}_6$: C, 40.19; H, 6.18; N, 18.23. Found: C, 40.26; H, 6.09; N, 18.28. Physicochemical data, including UV-vis, ESI-MS, EPR, ^{13}C NMR and ^1H NMR, were reported in Figs. S15–S18. UV-vis in CH_3CN (Fig. S15): $\lambda_{\text{max}}(\epsilon) = 415\text{ nm}$ ($870\text{ M}^{-1}\text{ cm}^{-1}$) and 610 nm ($220\text{ M}^{-1}\text{ cm}^{-1}$). ESI-MS in CH_3CN (Fig. S16a): m/z 438.3 for $[\text{Co}^{\text{III}}(\text{Me}_3\text{-TPADP})(\text{OO}^t\text{Bu})(\text{N}_3)]^+$ (calcd $m/z = 438.2$). EPR silent spectrum (Fig. S17a) and ^1H NMR spectral features (Fig. S18b) in diamagnetic region (0–10 ppm) exhibit that **4** is a low-spin $S = 0$ cobalt(III) species. ^{13}C NMR (acetone- d_6 , 400 MHz, 233K) δ , ppm: 164.0 (pyC $_{\alpha}$), 141.2 (pyC $_{\gamma}$), 119.7 (pyC $_{\beta}$), 76.6 (O-C-(CH $_3$) $_3$), 72.3 (py-CH $_2$), 67.7, 59.5 (N-CH $_2$ -CH $_2$), 49.1 (N-CH $_3$), 46.2 (N-CH $_3$), 27.3 (O-C-(CH $_3$) $_3$); ^1H NMR (acetone- d_6 , 400 MHz, 233K) δ , ppm: 8.21 (t, 1H, pyH $_{\gamma}$), 7.66 (d, 2H, pyH $_{\beta}$), 4.56–4.34 (m, 4H, py-CH $_2$), 3.49–2.62 (m, 8H, N-CH $_2$ -CH $_2$), 3.38 (s, 6H, N-CH $_3$), 2.52 (s, 3H, N-CH $_3$), 1.02 (s, 9H, O-C-(CH $_3$) $_3$).

Synthesis and Characterization of $[\text{Co}^{\text{III}}(\text{Me}_3\text{-TPADP})(\text{OO}^t\text{Bu})(\text{NCS})](\text{ClO}_4)$ (5-ClO₄**).**

Treatment of **1**-(ClO $_4$) $_2$ (0.05 mmol) with 5 equiv of $^t\text{BuOOH}$ and 2 equiv of TEA in the presence of 1.1 equiv of NaNCS in $\text{CH}_3\text{CN}/\text{MeOH}$ ($v/v = 1:1$, 2 mL) afforded the formation of a light purple solution at $20\text{ }^\circ\text{C}$. Et $_2\text{O}$ (40 mL) was added to the resulting solution to yield a light purple powder, which was washed with Et $_2\text{O}$, and dried in vacuo. Light purple powder dissolved in $\text{CH}_3\text{CN}/\text{MeOH}$ ($v/v = 1:1$). After the resulting solution was filtered, X-ray crystallographically suitable light purple crystals, $[\text{Co}^{\text{III}}(\text{Me}_3\text{-TPADP})(\text{OO}^t\text{Bu})(\text{NCS})](\text{ClO}_4)(\text{CH}_3\text{CN})$ (**5-ClO₄·CH₃CN**), were obtained by standing for several days at $-40\text{ }^\circ\text{C}$. Crystalline yield: 0.0094 g (41%). Anal. Calcd for $\text{C}_{19}\text{H}_{33}\text{ClCoN}_5\text{O}_6\text{S}$: C, 41.20; H, 6.00; N, 12.64. Found: C, 40.73; H, 6.05; N, 12.61. Physicochemical data, including UV-vis, ESI-MS, EPR, ^{13}C NMR and ^1H NMR, were reported in Figs. S15–S17, and S19. UV-vis in CH_3CN (Fig. S15): $\lambda_{\text{max}}(\epsilon) = 415\text{ nm}$ ($580\text{ M}^{-1}\text{ cm}^{-1}$) and 540 nm ($230\text{ M}^{-1}\text{ cm}^{-1}$). ESI-MS in CH_3CN (Fig. S16b): m/z 454.2 for $[\text{Co}^{\text{III}}(\text{Me}_3\text{-TPADP})(\text{OO}^t\text{Bu})(\text{NCS})]^+$ (calcd $m/z = 454.2$). EPR silent spectrum (Fig. S17b) and ^1H NMR spectral features (Fig. S19b) in diamagnetic region (0–10 ppm) demonstrate

that **5** is a low-spin $S = 0$ cobalt(III) species. ^{13}C NMR (acetone- d_6 , 400 MHz, 233K) δ , ppm: 164.2 (pyC $_{\alpha}$), 141.6 (pyC $_{\gamma}$), 140.5 (N-CS) 120.0 (pyC $_{\beta}$), 76.7 (O-C-(CH $_3$) $_3$), 72.1 (py-CH $_2$), 68.2, 59.4 (N-CH $_2$ -CH $_2$), 50.6 (N-CH $_3$), 48.2 (N-CH $_3$), 27.0 (O-C-(CH $_3$) $_3$); ^1H NMR (acetone- d_6 , 400 MHz, 233K) δ , ppm: 8.23 (t, 1H, pyH $_{\gamma}$), 7.66 (d, 2H, pyH $_{\beta}$), 4.67-4.49 (m, 4H, py-CH $_2$), 3.85-2.80 (m, 8H, N-CH $_2$ -CH $_2$), 3.38 (s, 6H, N-CH $_3$), 2.75 (s, 3H, N-CH $_3$), 0.95 (s, 9H, O-C-(CH $_3$) $_3$).

X-ray Crystallography. Single crystals of **2**-BPh $_4$ ·Et $_2$ O, **4**-ClO $_4$, and **5**-ClO $_4$ ·CH $_3$ CN were picked from solutions by a nylon loop (Hampton Research Co.) on a handmade copper plate mounted inside a liquid N $_2$ Dewar vessel at *ca.* -40 °C and mounted on a goniometer head in a N $_2$ cryostream. Data collections were carried out on a Bruker SMART APEX II CCD diffractometer equipped with a monochromator in the Mo K α ($\lambda = 0.71073$ Å) incident beam. The CCD data were integrated and scaled using the Bruker-S SAINT software package, and the structure was solved and refined using SHELXTL V 6.12.³ Hydrogen atoms were located in the calculated positions. All non-hydrogen atoms were refined with anisotropic thermal parameters. The crystallographic data with the selected bond distances and angles for **2**-BPh $_4$ ·Et $_2$ O, **4**-ClO $_4$, and **5**-ClO $_4$ ·CH $_3$ CN are listed in Table S2. CCDC-1906995 for **2**-BPh $_4$ ·Et $_2$ O, CCDC-1906994 for **4**-ClO $_4$, and CCDC-1906996 for **5**-ClO $_4$ ·CH $_3$ CN contain the supplementary crystallographic data for this paper. These data can be obtained free of charge via www.ccdc.cam.ac.uk/data_request/cif (or from the Cambridge Crystallographic Data Centre, 12, Union Road, Cambridge CB2 1EZ, UK; fax: (+44) 1223-336-033; or deposit@ccdc.cam.ac.uk).

Reactivity Studies. All reactions were performed in a 1-cm UV cuvette by monitoring UV-vis spectral changes of reaction solutions, and rate constants were determined by fitting the changes in absorbance of 360 nm for reaction of [Co^{III}(Me $_3$ -TPADP)(OO^tBu) $_2$]⁺ (**2**) with 2-phenylpropionaldehyde (2-PPA), 400 nm for reaction of **2** with *para*-substituted benzaldehydes (*para*-X-Ph-CHO; X = Me, F, H, Cl, and CF $_3$), and 530 nm for reaction of **2** with 1-pentanal, 2-methylbutanal, and pivalaldehyde. Reactions were run at least in triplicate,

and the data reported represent the average of these reactions. *In-situ*-generated **2** was used in kinetic studies, such as the oxidation of *para*-substituted benzaldehydes (*para*-X-Ph-CHO; X = Me, F, H, Cl, and CF₃) in CH₃CN/MeOH (*v/v* = 3:1) at 15 °C (Fig. 3a–3b and Table S3), 1-pentanal, 2-methylbutanal, and pivalaldehyde in CH₃CN/MeOH (*v/v* = 3:1) at 25 °C (Fig. S8), and 2-PPA in CH₃CN at 25 °C (Figs. S9 and S10). After the completion of reactions, pseudo-first-order fitting of the kinetic data allowed us to determine *k*_{obs} values. Products formed in the oxidation of benzaldehyde and 2-PPA by **2** were analyzed by injecting the reaction mixture directly into GC. Products were identified by comparison with authentic samples, and product yields were determined by comparison against standard curves prepared with authentic samples.

References

1. B. Shin, K. D. Sutherlin, T. Ohta, T. Ogura, E. I. Solomon, J. Cho, *Inorg. Chem.*, 2016, **55**, 12391–12399.
2. D. F. Evans, D. A. Jakubovic, *J. Chem. Soc., Dalton Trans.*, 1988, 2927–2933.
3. Sheldrick, G. M. *SHELXTL/PC*. Version 6.12 for Windows XP; Bruker AXS Inc.; Madison, WI, 2001.

Table S1. Crystal Data and Structure Refinements for **2-BPh₄·Et₂O**, **4-ClO₄**, and **5-ClO₄·CH₃CN**

	2-BPh₄·Et₂O	4-ClO₄	5-ClO₄·CH₃CN
Empirical formula	C ₅₀ H ₇₂ BCoN ₄ O ₅	C ₁₈ H ₃₃ ClCoN ₇ O ₆	C ₂₁ H ₃₆ ClCoN ₆ O ₆ S
Formula weight	878.85	537.89	595.00
Temperature (K)	293.0(2)	153.0(2)	293.0(2)
Wavelength (Å)	0.71073	0.71073	0.71073
Crystal system/space group	Monoclinic, <i>P2/c</i>	Monoclinic, <i>Cc</i>	orthorhombic, <i>P_{bca}</i>
Unit cell dimensions			
<i>a</i> (Å)	12.353(4)	17.659(11)	9.177(7)
<i>b</i> (Å)	23.359(5)	11.390(8)	17.401(12)
<i>c</i> (Å)	16.581(5)	12.836(8)	33.72(3)
α (°)	90	90	90
β (°)	92.432(14)	115.338(16)	90
γ (°)	90	90	90
Volume (Å ³)	4780.0(2)	2333.0(3)	5385.0(7)
<i>Z</i>	4	4	8
Calculated density (g/cm ⁻³)	1.221	1.531	1.68
Absorption coefficient (mm ⁻¹)	0.408	0.900	0.861
Reflections collected	185213	34155	128191
Independent reflections [<i>R</i> (int)]	11829 [0.0923]	5785 [0.0529]	4738 [0.2317]
Refinement method	Full-matrix least-squares on <i>F</i> ²	Full-matrix least-squares on <i>F</i> ²	Full-matrix least-squares on <i>F</i> ²
Data/restraints/parameters	11829/0/561	5785/2/304	4738/0/332
Goodness-of-fit on <i>F</i> ²	0.990	0.844	1.133
Final <i>R</i> indices [<i>I</i> > 2σ(<i>I</i>)]	<i>R</i> ₁ = 0.0432, <i>wR</i> ₂ = 0.1225	<i>R</i> ₁ = 0.0353, <i>wR</i> ₂ = 0.0993	<i>R</i> ₁ = 0.0771, <i>wR</i> ₂ = 0.1278
<i>R</i> indices (all data)	<i>R</i> ₁ = 0.0673, <i>wR</i> ₂ = 0.1387	<i>R</i> ₁ = 0.0449, <i>wR</i> ₂ = 0.1090	<i>R</i> ₁ = 0.1337, <i>wR</i> ₂ = 0.1460
Largest difference peak and hole (e/Å ³)	0.446 and -0.443	0.268 and -0.299	0.686 and -0.561

Table S2. Selected Bond Distances (Å) and Angles (°) for **2-BPh₄·Et₂O**, **4-ClO₄**, and **5-ClO₄·CH₃CN**

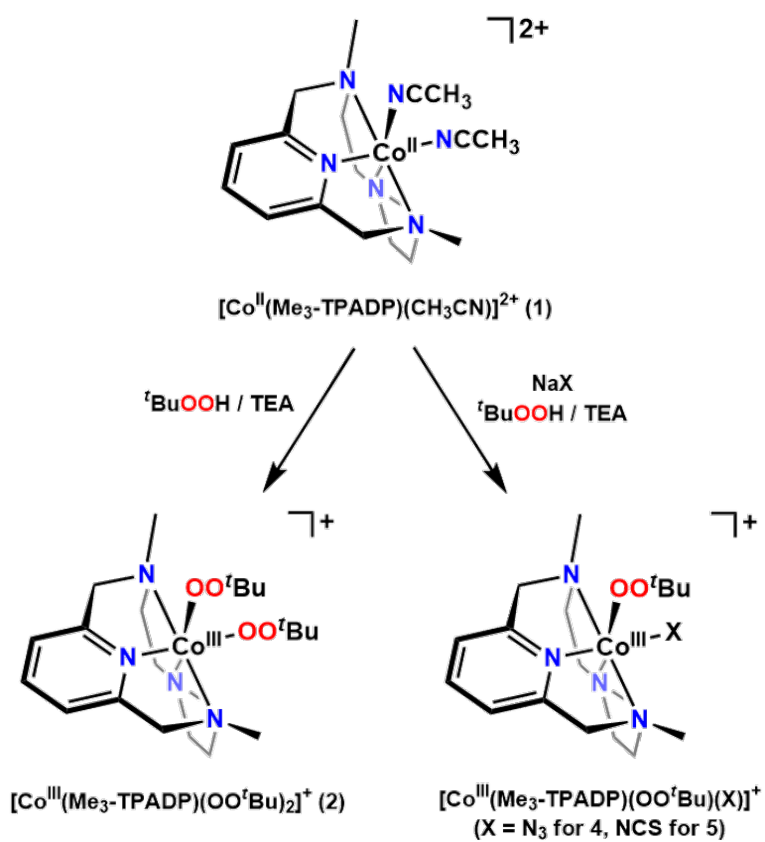
Bond Distances (Å)					
2-BPh ₄ ·Et ₂ O		4-ClO ₄		5-ClO ₄ ·CH ₃ CN	
Co–O1	1.8604(12)	Co–O1	1.862(3)	Co–O1	1.880(4)
Co–O3	1.8575(12)	Co–N1	2.037(3)	Co–N1	2.053(5)
Co–N1	2.0386(15)	Co–N2	2.011(4)	Co–N2	2.009(5)
Co–N2	2.0113(16)	Co–N3	1.878(3)	Co–N3	1.858(4)
Co–N3	1.9018(14)	Co–N4	2.015(4)	Co–N4	2.007(5)
Co–N4	2.0459(16)	Co–N5	1.943(4)	Co–N5	1.880(5)
O1–O2	1.4847(17)	O1–O2	1.479(4)	O1–O2	1.430(6)
O3–O4	1.4667(17)				
Bond Angles (°)					
2-BPh ₄ ·Et ₂ O		4-ClO ₄		5-ClO ₄ ·CH ₃ CN	
N1–Co–N2	86.53(6)	N1–Co–N2	86.26(15)	N1–Co–N2	85.7(2)
N1–Co–N3	93.43(6)	N1–Co–N3	92.98(14)	N1–Co–N3	94.24(19)
N1–Co–N4	86.63(6)	N1–Co–N4	86.31(15)	N1–Co–N4	86.14(19)
N1–Co–O1	174.41(6)	N1–Co–N5	89.51(14)	N1–Co–N5	89.9(2)
N1–Co–O3	88.27(6)	N1–Co–O1	174.91(14)	N1–Co–O1	174.27(19)
N2–Co–N3	83.35(6)	N2–Co–N3	83.61(15)	N2–Co–N3	83.8(2)
N2–Co–N4	164.19(6)	N2–Co–N4	165.02(14)	N2–Co–N4	164.82(19)
N2–Co–O1	92.02(6)	N2–Co–N5	96.16(16)	N2–Co–N5	97.5(2)
N2–Co–O3	87.47(6)	N2–Co–O1	91.79(15)	N2–Co–O1	99.8(2)
N3–Co–N4	82.85(6)	N3–Co–N4	83.80(14)	N3–Co–N4	84.1(2)
N3–Co–O1	91.76(6)	N3–Co–N5	177.48(15)	N3–Co–N5	175.8(2)
N3–Co–O3	170.55(6)	N3–Co–O1	91.47(14)	N3–Co–O1	87.91(19)
N4–Co–O1	96.08(6)	N4–Co–N5	96.77(15)	N4–Co–N5	95.2(2)
N4–Co–O3	106.54(6)	N4–Co–O1	96.62(15)	N4–Co–O1	88.8(2)
O1–Co–O3	86.28(6)	N5–Co–O1	86.03(14)	N5–Co–O1	87.9(2)
Co–O1–O2	112.48(8)	Co–O1–O2	113.3(2)	Co–O1–O2	111.6(3)
Co–O3–O4	115.16(9)	Co–N5–N6	119.5(3)	Co–N5–C15	161.5(5)

Table S3. Kinetic data for the oxidation of *para*-substituted benzaldehydes (200 equiv) by **2** (0.5 mM) in CH₃CN/MeOH (*v/v* = 3:1) at 15 °C

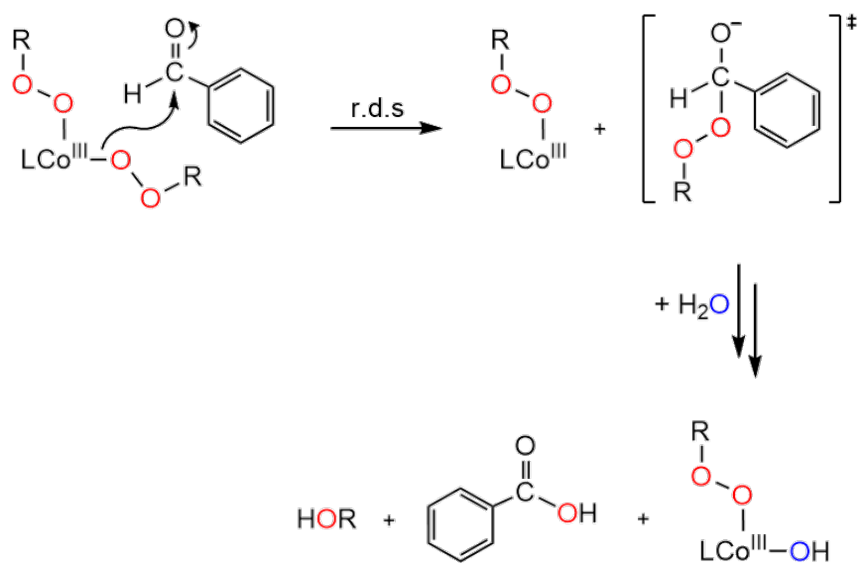
Substrate	2 k_{obs} (s ⁻¹)
<i>p</i> -tolualdehyde	$3.2(1) \times 10^{-3}$
4-fluorobenzaldehyde	$3.3(2) \times 10^{-3}$
benzaldehyde	$3.6(1) \times 10^{-3}$
4-chlorobenzaldehyde	$3.8(1) \times 10^{-3}$
4-(trifluoromethyl)benzaldehyde	$5.9(3) \times 10^{-3}$

Table S4. Product analysis for the oxidation of 50 equiv of aldehydes (1-pentanal (1°-CHO), 2-methylbutanal (2°-CHO), and pivalaldehyde (3°-CHO)) by **2** (0.5 mM) in CH₃CN/MeOH (v/v = 3:1) at 25 °C

Entry	Substrate	Oxidation product	Oxidation product % yield
1	1-pentanal	pentanoic acid	94(3)
2	2-methylbutanal	2-methylbutanoic acid	94(4)
3	pivalaldehyde	2,2-dimethylpropanoic acid	94(1)



Scheme S1. Synthetic procedures for $Co^{III}-(OO^tBu)_2$ and $Co^{III}-(OO^tBu)(X)$ complexes (X = N₃ or NCS).



Scheme S2. Proposed mechanism for the oxidation of benzaldehyde with complex **2** (L = Me₃-TPADP, R = ^tBu).

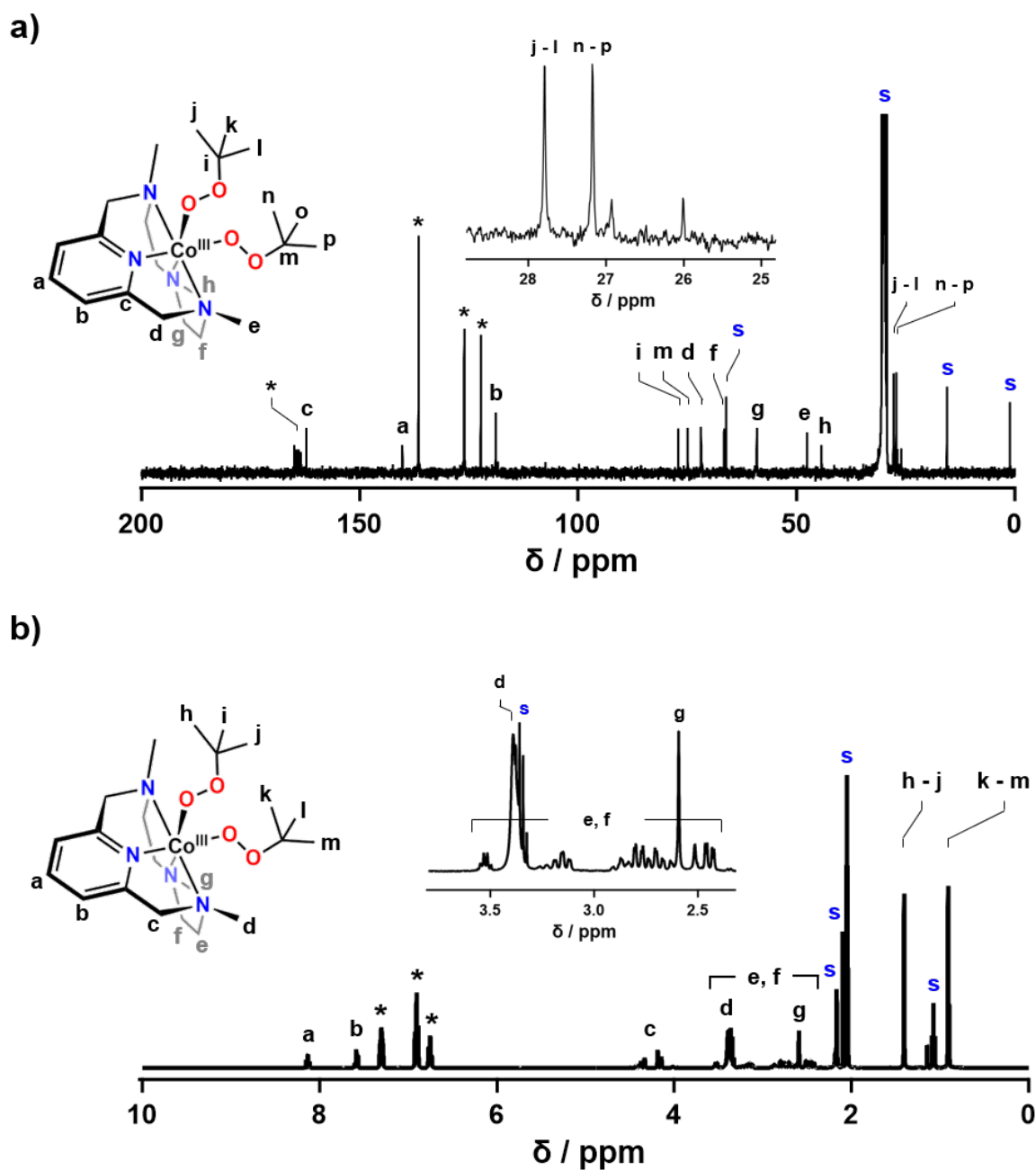


Figure S1. (a) The ¹³C NMR spectrum of [Co^{III}(Me₃-TPADP)(OO^tBu)₂]⁺ (**2**) in acetone-*d*₆ at -40 °C. (b) The ¹H NMR spectrum of **2** in diamagnetic region at -40 °C in acetone-*d*₆. The peaks marked with ‘s’ and ‘*’ are ascribed to solvents and a counter anion (BPh₄⁻), respectively. The 2 – 4 ppm region shows the d – g peaks together with some unidentified signals due to the thermal instability of **2**.

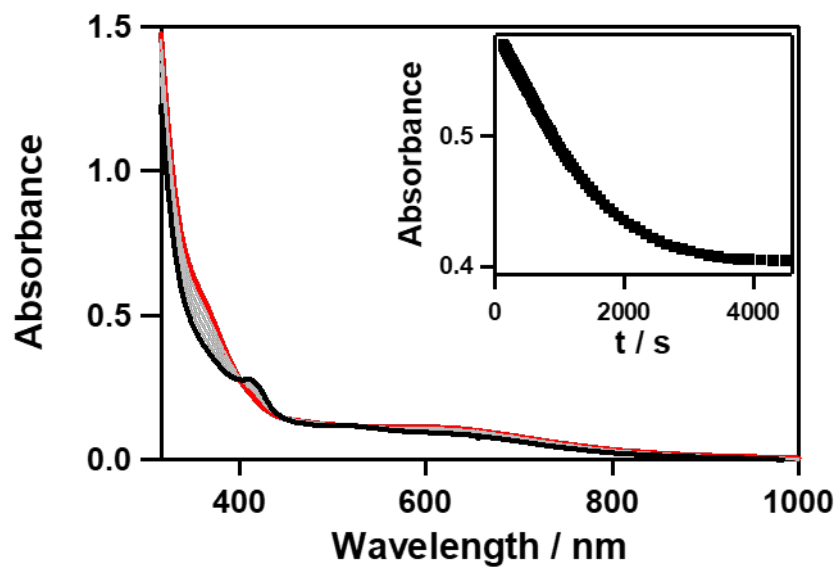


Figure S2. UV-vis spectral changes of **2** (0.5 mM) upon natural decay at 25 °C under an inert atmosphere. Inset shows the time course of the absorbance at 360 nm.

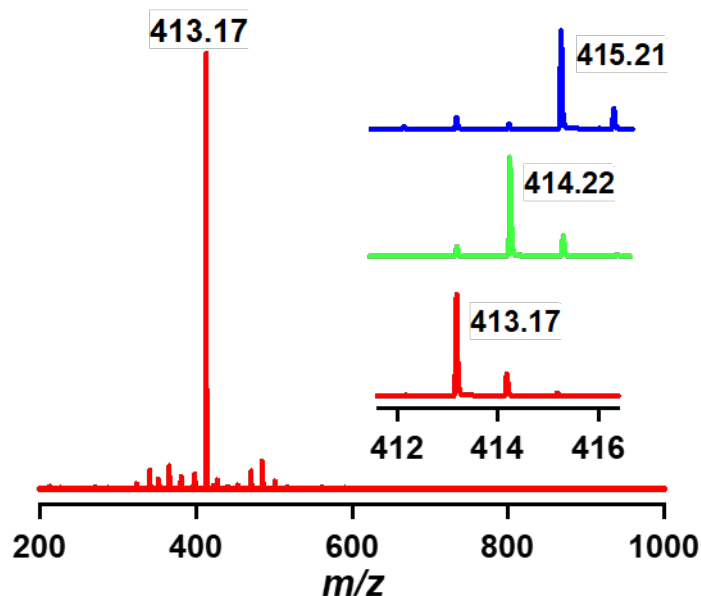


Figure S3. CSI-MS taken after the completion of thermal decay of **2** in acetone at 25 °C under an inert atmosphere, showing the formation of $\text{Co}^{\text{III}}\text{-(OO'Bu)(OH)}$ complex, $[\text{Co}^{\text{III}}(\text{Me}_3\text{-TPADP})(\text{OO'Bu})(\text{OH})]^+$ (**3**): Mass peak at 413.17 is assigned as $[\text{Co}^{\text{III}}(\text{Me}_3\text{-TPADP})(\text{OO'Bu})(\text{OH})]^+$ (calcd m/z 413.20). Insets show the observed isotope distribution patterns for $[\text{Co}^{\text{III}}(\text{Me}_3\text{-TPADP})(\text{OO'Bu})(\text{OH})]^+$ (red line), $[\text{Co}^{\text{III}}(\text{Me}_3\text{-TPADP})(\text{OO'Bu})(\text{OD})]^+$ (green line, calcd m/z 414.20), $[\text{Co}^{\text{III}}(\text{Me}_3\text{-TPADP})(\text{OO'Bu})(^{18}\text{OH})]^+$ (blue line, calcd m/z 415.20). $\text{Co}^{\text{III}}\text{-(OO'Bu)(OD)}$ complex and $\text{Co}^{\text{III}}\text{-(OO'Bu)(}^{18}\text{OH)}$ complex are generated by adding excess amount of D_2O and H_2^{18}O in **3**, respectively.

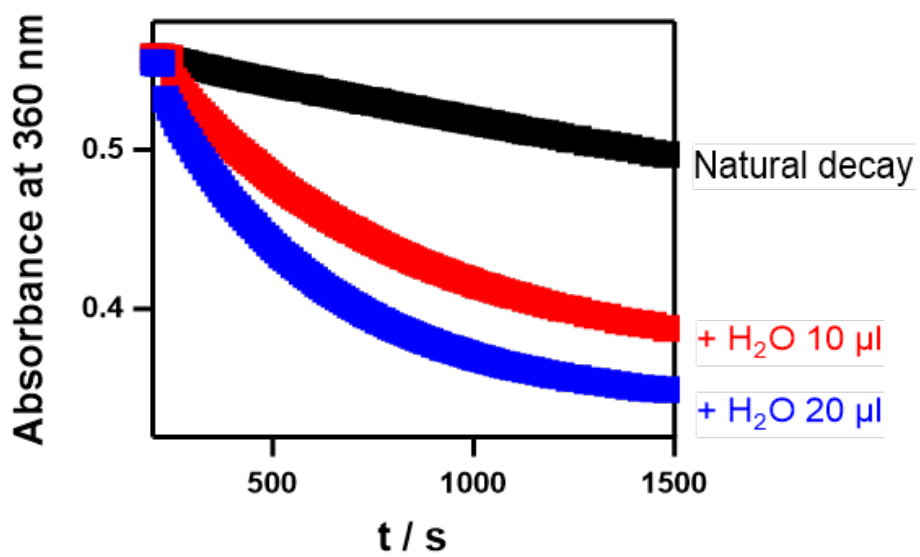


Figure S4. Time courses indicate the rate of decomposition upon addition of 0 μL (black), 10 μL (red) and 20 μL (blue) of H_2O to the solution of **2** for 1500 s. The rate of decomposition depends on the concentration of water.

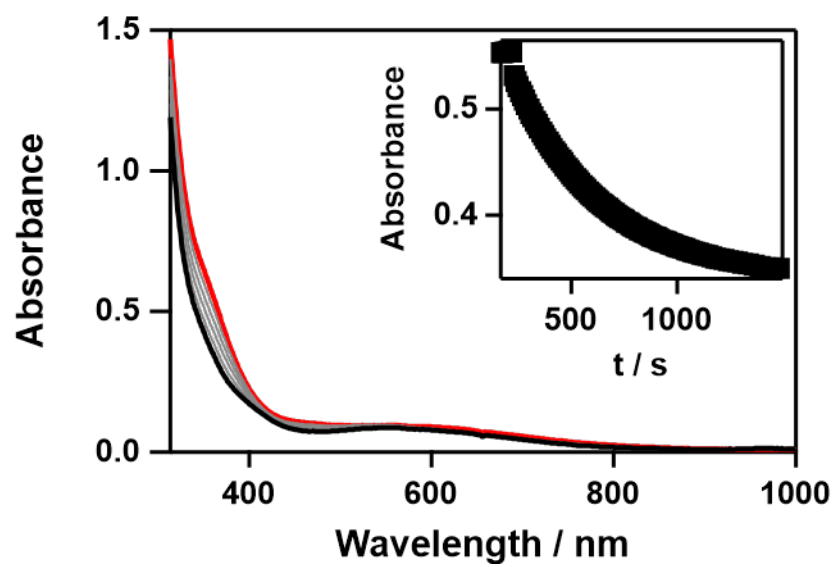


Figure S5. UV-vis spectral changes of **2** (0.5 mM) upon addition of 20 μL of H₂O at 25 °C. Inset shows the time course of the absorbance at 360 nm.

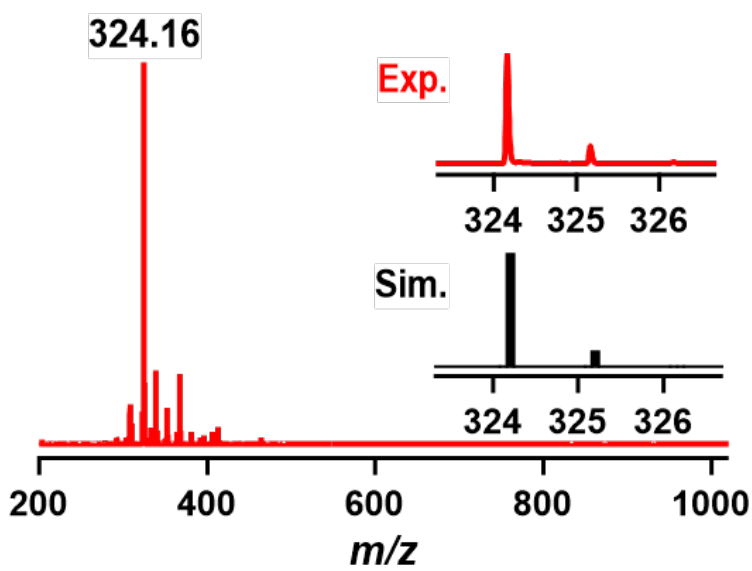


Figure S6. CSI-MS taken after the completion of the reaction of **2** with 20 μL of H_2O in acetonitrile at 25 $^\circ\text{C}$, showing the formation of cobalt(II)-hydroxo complex: Mass peak at 324.16 is assigned as $[\text{Co}^{\text{II}}(\text{Me}_3\text{-TPADP})(\text{OH})]^+$ (calcd m/z 324.14). Insets show its experimental (upper) and calculated (lower) isotope distribution patterns.

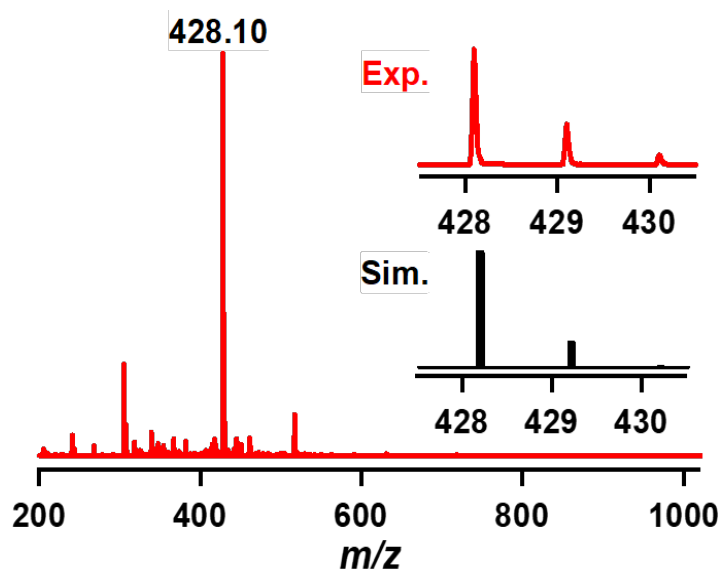


Figure S7. CSI-MS taken after the completion of the reaction of **2** with benzaldehyde in $\text{CH}_3\text{CN}/\text{MeOH}$ ($v/v = 3:1$) at 15°C under an inert atmosphere, showing the formation of cobalt(II)–benzoato complex: Mass peak at 428.10 is assigned as $[\text{Co}^{\text{II}}(\text{Me}_3\text{-TPADP})(\text{C}_6\text{H}_5\text{COO})]^+$ (calcd m/z 428.16). Insets show its experimental (upper) and calculated (lower) isotope distribution patterns.

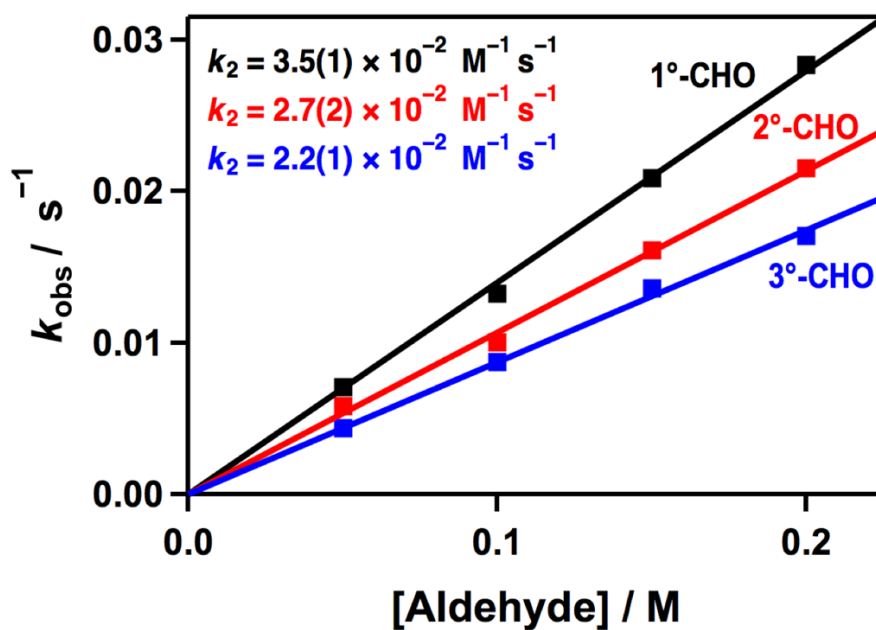


Figure S8. Plots of k_{obs} against aldehydes (1-pentanal (1°-CHO; black squares), 2-methylbutanal (2°-CHO; red squares), and pivalaldehyde (3°-CHO; blue squares)) concentration to determine a second-order rate constant of **2** in CH₃CN/MeOH ($v/v = 3:1$) at 25 °C.

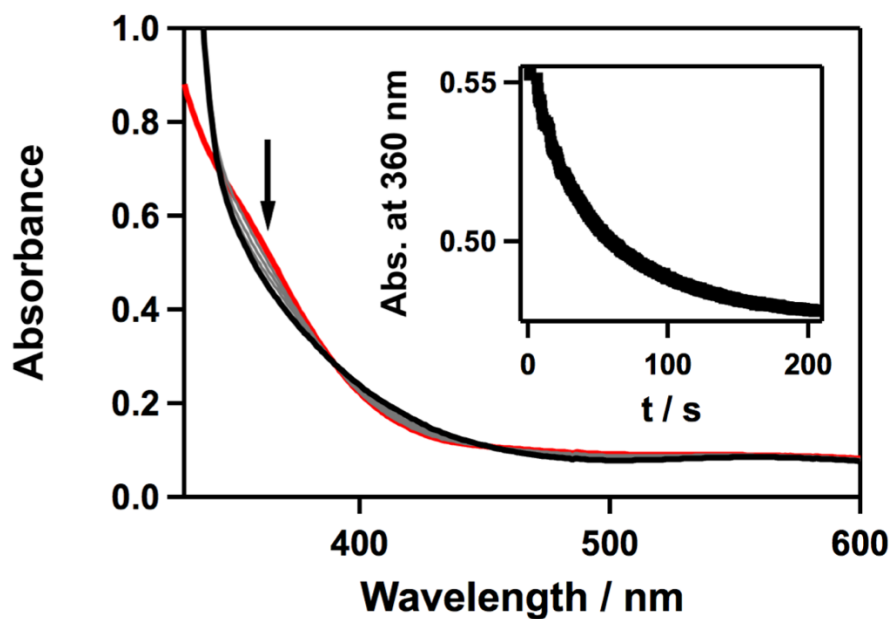


Figure S9. Reactions of **2** with 2-PPA in CH₃CN. UV-vis spectral changes of **2** (0.5 mM) upon addition of 200 equiv of 2-PPA at 25 °C. Inset shows the time course of the absorbance at 360 nm.

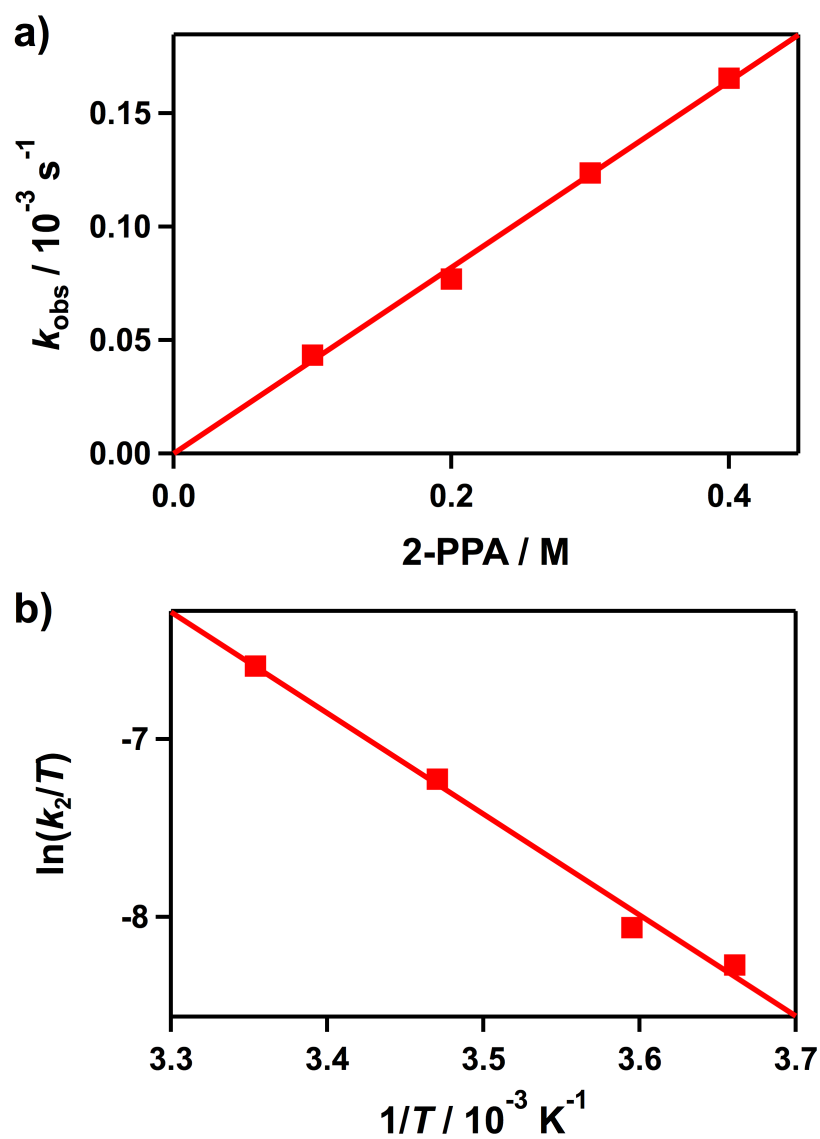


Figure S10. Reactions of $[\text{Co}^{\text{III}}(\text{Me}_3\text{-TPADP})(\text{OO}^t\text{Bu})_2]^+$ (**2**) with 2-PPA in CH_3CN . (a) Plot of k_{obs} against 2-PPA concentration to determine a second-order rate constant of **2** at 25 °C. (b) Plot of second-order rate constants against $1/T$ to determine activation parameters for the reaction of **2** (0.5 mM) and 2-PPA.

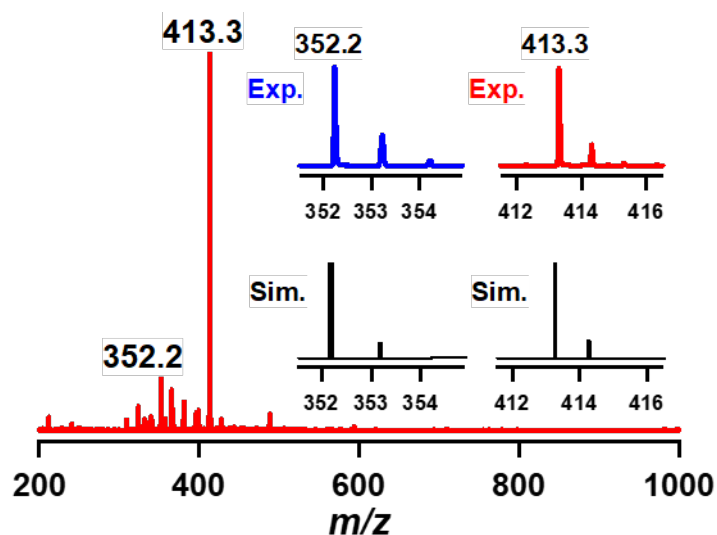


Figure S11. CSI-MS taken after the completion of the reaction of **2** with 2-PPA in CH₃CN at 25 °C under an inert atmosphere, showing the formation of **3**: Mass peak at m/z 413.3 is assigned as [Co^{III}(Me₃-TPADP)(OO^tBu)(OH)]⁺ (**3**) (calcd m/z 413.2). In addition, mass peak at m/z 352.2 is assigned as [Co^{II}(Me₃-TPADP)(OOCH)]⁺ (calcd m/z 352.1), which was probably derived from the aldehyde deformylation of 2-PPA and small amount of decomposition of **2** during the reaction. Insets show its experimental (upper) and calculated (lower) isotope distribution patterns.

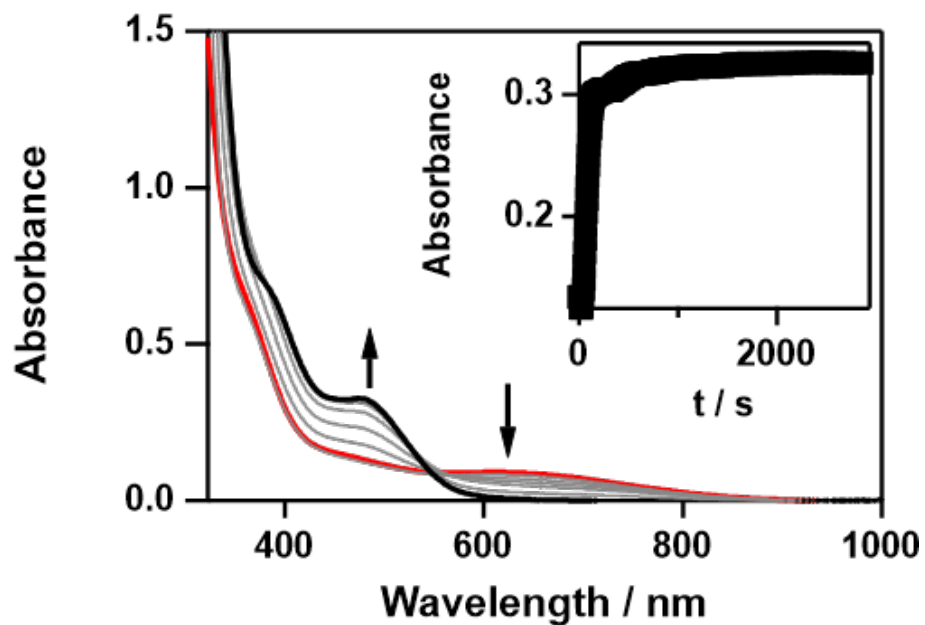


Figure S12. Reactions of isolated **2** with 2-PPA in CH₃CN under N₂. UV-vis spectral changes of **2** (0.5 mM) upon addition of 20 equiv of 2-PPA at 25 °C. Inset shows the time course of the absorbance at 480 nm.

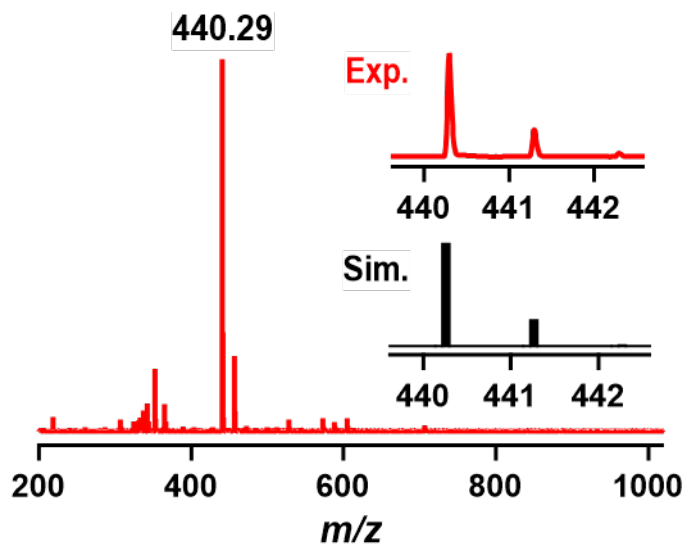


Figure S13. CSI-MS taken after the completion of the reaction of isolated **2** with 2-PPA in CH_3CN at 25 °C under N_2 atmosphere, showing the formation of cobalt(II)-enolato complex: Mass peak at m/z 440.29 is assigned as $[\text{Co}^{\text{II}}(\text{Me}_3\text{-TPADP})(\text{OCH}=\text{C}(\text{Me})\text{Ph})]^+$ (calcd m/z 440.2). Insets show its experimental (upper) and calculated (lower) isotope distribution patterns.

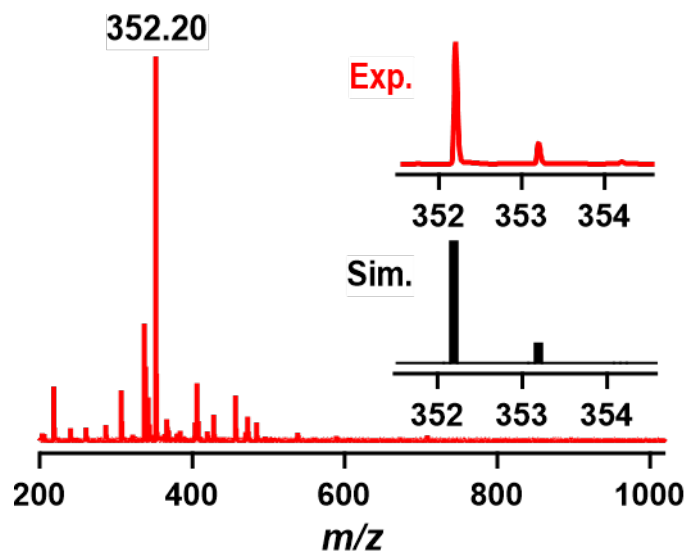


Figure S14. CSI-MS taken after the O₂ bubbling to the cobalt(II)-enolato complex solution in CH₃CN at 25 °C under N₂, showing the formation of cobalt(II) formate species: Mass peak at *m/z* 352.20 is assigned as [Co^{II}(Me₃-TPADP)(OOCH)]⁺ (calcd *m/z* 352.13). Insets show its experimental (upper) and calculated (lower) isotope distribution patterns.

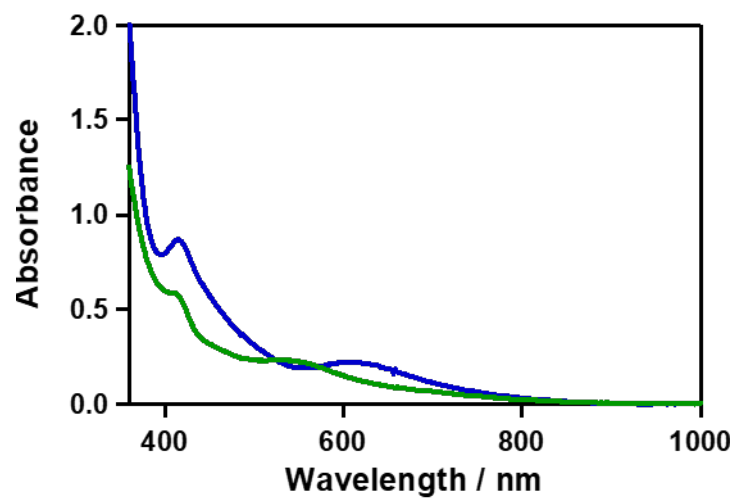


Figure S15. UV-vis spectra of $[\text{Co}^{\text{III}}(\text{Me}_3\text{-TPADP})(\text{OO}'\text{Bu})(\text{N}_3)]^+$ (**4**) (blue line) and $[\text{Co}^{\text{III}}(\text{Me}_3\text{-TPADP})(\text{OO}'\text{Bu})(\text{NCS})]^+$ (**5**) (green line) in CH_3CN at $25\text{ }^\circ\text{C}$.

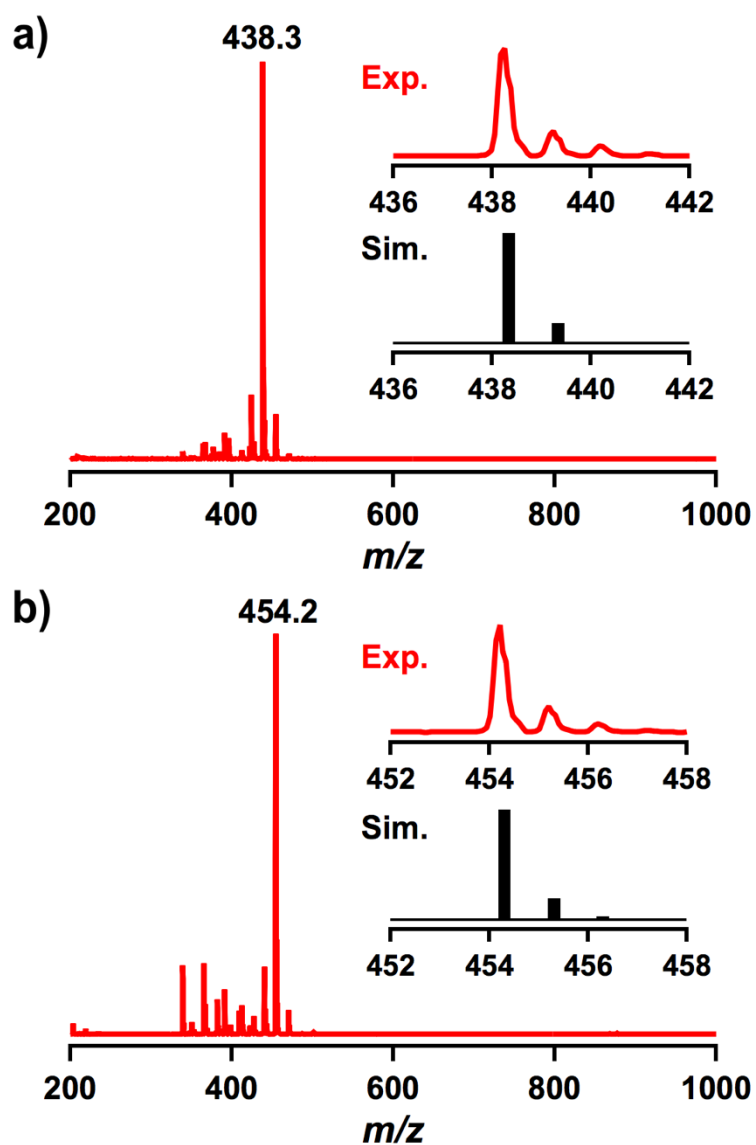


Figure S16. ESI-MS of (a) $[Co^{III}(Me_3-TPADP)(OO'Bu)(N_3)]^+$ (4) and (b) $[Co^{III}(Me_3-TPADP)(OO'Bu)(NCS)]^+$ (5) in CH_3CN at 25 °C. Insets show experimental (upper) and calculated (lower) isotope distribution patterns.

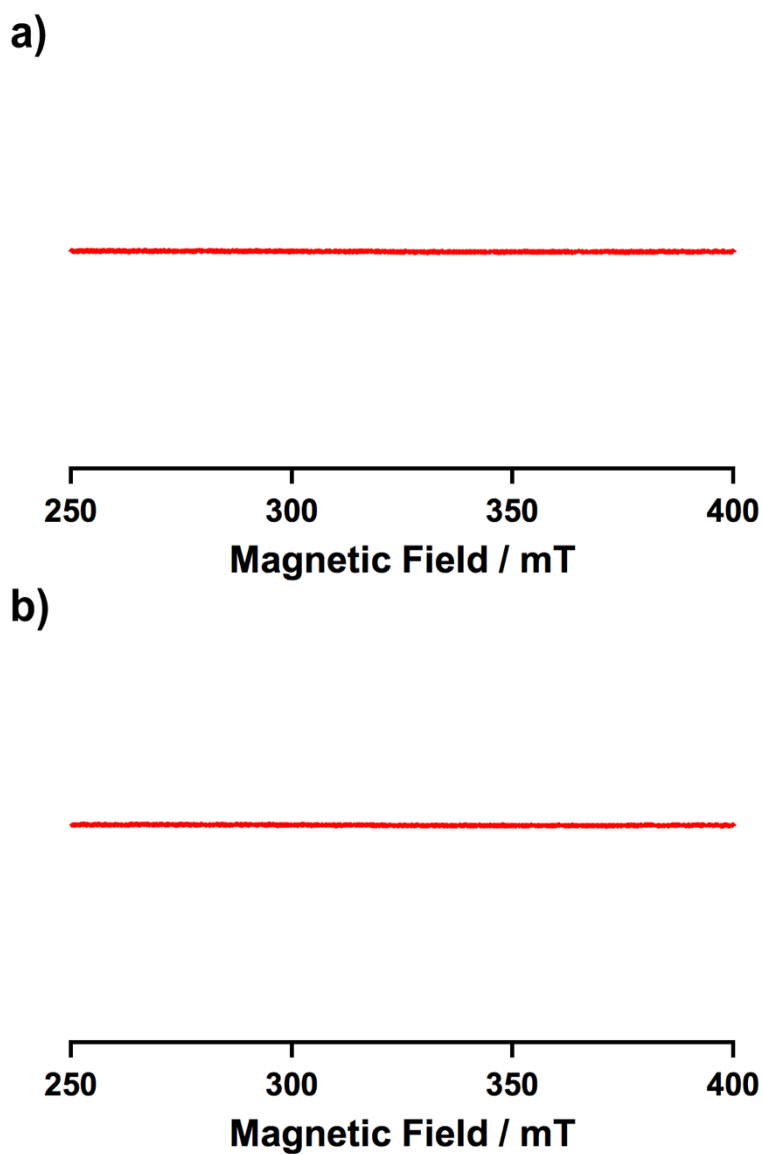


Figure S17. X-band EPR spectra of (a) $[\text{Co}^{\text{III}}(\text{Me}_3\text{-TPADP})(\text{OO}'\text{Bu})(\text{N}_3)]^+$ (**4**) and (b) $[\text{Co}^{\text{III}}(\text{Me}_3\text{-TPADP})(\text{OO}'\text{Bu})(\text{NCS})]^+$ (**5**). The parameters for measurement of (a): microwave power = 1.0 mW, frequency = 9.155 GHz, sweep width = 0.25 T, modulation amplitude = 0.60 mT. The parameters for measurement of (b): microwave power = 1.0 mW, frequency = 9.159 GHz, sweep width = 0.25 T, modulation amplitude = 0.60 mT.

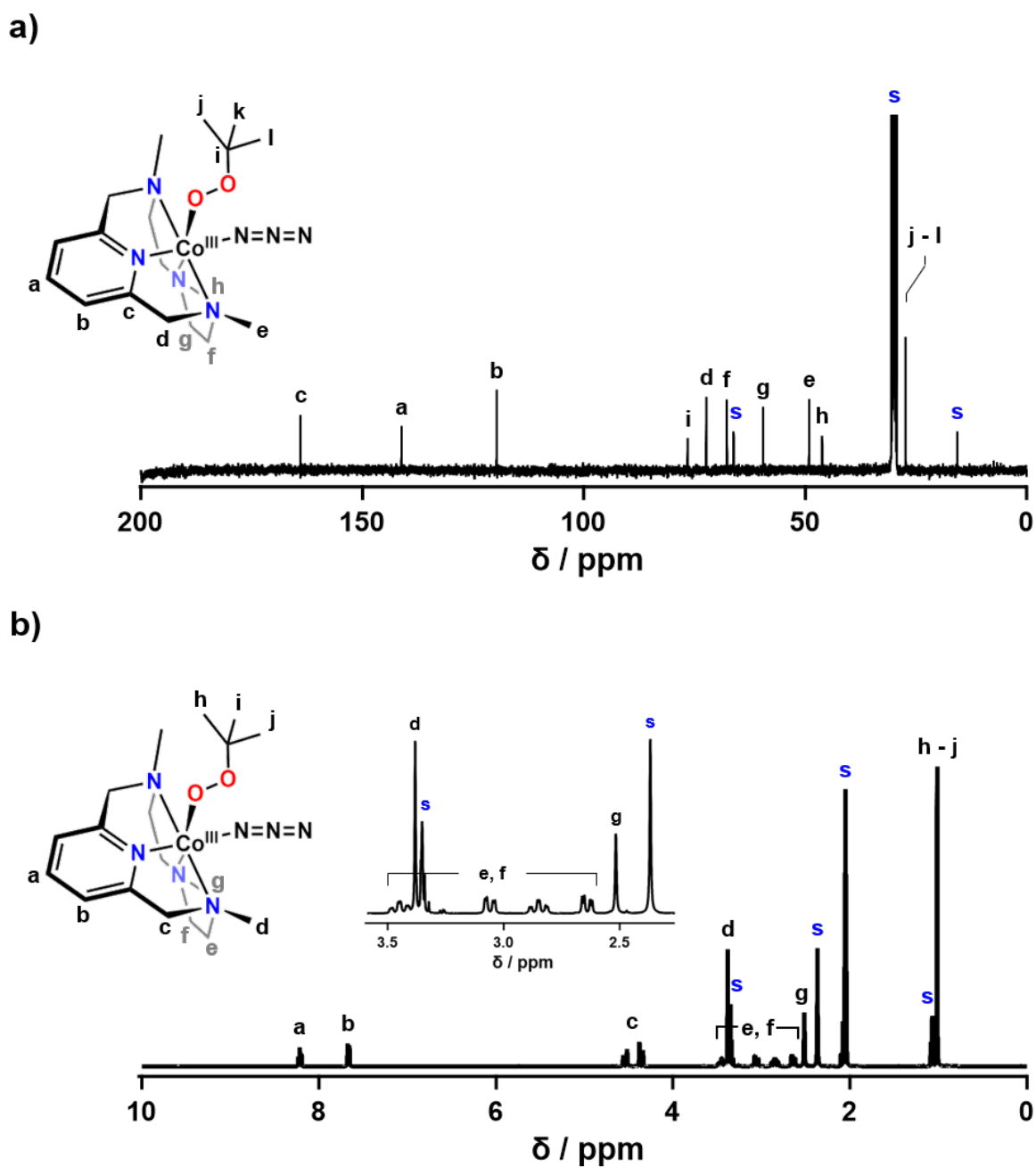


Figure S18. (a) The ^{13}C NMR spectrum of $[\text{Co}^{\text{III}}(\text{Me}_3\text{-TPADP})(\text{OO}^t\text{Bu})(\text{N}_3)]^+$ (**4**) in acetone- d_6 at $-40\text{ }^\circ\text{C}$. (b) The ^1H NMR spectrum of **4** in diamagnetic region at $-40\text{ }^\circ\text{C}$ in acetone- d_6 . The peaks marked with ‘s’ are ascribed to solvents.

